Liquid-liquid phase separation recapitulates the thermodynamics and kinetics of heterochromatin formation

Maxime M.C. Tortora[1,*], Lucy Brennan[2], Gary Karpen[2,3,*], Daniel Jost[1,*]

[1]Laboratoire de Biologie et Modélisation de la Cellule, École Normale Supérieure de Lyon, CNRS, UMR5239, Inserm U1293, Université Claude Bernard Lyon 1, Lyon, France
[2]Department of Molecular and Cell Biology, University of California, Berkeley, CA, USA
[3]BioEngineering and BioMedical Sciences Department, Lawrence Berkeley National Laboratory, Berkeley, CA, USA
[*]co-corresponding authors. Modeling: maxime.tortora@ens-lyon.fr ; daniel.jost@ens-lyon.fr ; Experiments: gkarpen@berkeley.edu

ABSTRACT

The spatial segregation of heterochromatin into distinct, membrane-less nuclear compartments involves the binding of the heterochromatin protein 1 (HP1) to H3K9me2/3-rich genomic regions. While HP1 exhibits liquid-liquid phase separation (LLPS) properties *in vitro*, its mechanistic role *in vivo* on the structure and dynamics of heterochromatin remains largely unresolved. Here, using biophysical modeling, we systematically investigate the mutual coupling between self-interacting HP1-like molecules and the chromatin polymer. We reveal that the specific affinity of HP1 for H3K9me2/3 loci facilitates coacervation *in nucleo*, and promotes the formation of stable heterochromatin condensates at HP1 levels far below the critical LLPS concentration observed *in vitro* in purified protein assays. These heterotypic HP1-chromatin interactions give rise to a strong dependence of the nucleoplasmic HP1 density on the HP1-H3K9me2/3 stoichiometry, consistent with the thermodynamics of multicomponent LLPS. The dynamical crosstalk between HP1 and the visco-elastic chromatin scaffold also leads to anomalously-slow equilibration kinetics, which may result in the coexistence of multiple long-lived, microphase-separated heterochromatin compartments. The morphology of these coacervates is further found to be governed by the dynamic establishment of the underlying H3K9me2/3 landscape, which may drive their increasingly abnormal, aspherical shapes during cell development. These findings compare favorably to 4D microscopy measurements of HP1 condensates that we perform in live *Drosophila* embryos, and suggest a general quantitative model of heterochromatin formation based on the interplay between LLPS and chromatin mechanics.

SIGNIFICANCE STATEMENT

The compartmentalization of heterochromatin, the constitutively silent part of the genome, into membrane-less organelles, enriched in HP1 proteins, is critical to both genetic stability and cell fate determination. While HP1 can self-organize into liquid-like condensates *in vitro*, its role in the formation of 3D heterochromatin domains *in vivo* is not fully understood. Using large-scale molecular simulations, we show that key kinetic and thermodynamic features of heterochromatin condensates may be reconciled with a liquid-liquid phase-separation (LLPS) mode of organization driven by the self-attraction of HP1 and its specific affinity for methylated chromatin. Our theoretical predictions are corroborated by live-microscopy experiments performed during early fly embryogenesis, suggesting that the strong crosstalk between HP1-based LLPS and chromosome mechanics is central to heterochromatin formation.

INTRODUCTION

The regulation of genome function in eukaryotes is a highly-complex biological process, which typically involves the combined contribution of hundreds of intra-nuclear proteins, DNA and RNA structures (1). The precise and coordinated recruitment of regulatory molecules at specific genomic or molecular targets often gives rise to spatially- and biochemically-distinct compartments, which play essential roles in a variety of cellular activities including DNA repair (2), transcription (3, 4), replication (5) and epigenetic regulation (6). These membrane-less condensates act as both organizational hubs and localized crucibles for the catalysis of multiple biochemical reactions involved in the translation and maintenance of genetic information (7). In recent years, the physical mechanism of liquid-liquid phase separation (LLPS) has been increasingly proposed as a unifying paradigm that can readily explain the formation of dynamic, functional compartments based on inherent interactions among proteins, nucleic acids (RNA and DNA), or other biomolecules (7, 8). For instance, spontaneous protein segregation into liquid-like supra-molecular assemblies can be driven by weak, multivalent affinity interactions among structured protein domains or large low-complexity, intrinsically-disordered regions (IDRs), which are commonly observed in many eukaryotic proteins (7, 9).

However, the difficulty of quantitatively and unequivocally distinguishing LLPS from alternative self-organization processes *in vivo* has generated disputes about its biological relevance (10–12). A particularly notable debate has focused on the case of pericentromeric heterochromatin, which forms large, distinct nuclear compartments required for chromosome folding and segregation, as well as for transcriptional silencing of transposons and genes (13). Pericentromeres are biochemically defined by genomic regions enriched in repeated DNA sequences, as well as in histone H3 lysine 9 di- or tri-methylation marks (H3K9me2/3) and their epigenetic "reader" protein, Heterochromatin Protein 1a/α (HP1a/α) (14). Careful genetic and biochemical studies have teased apart a hierarchy of interactions that contribute to the formation and maintenance of pericentromeric domains. The first level of interactions involves the dimerization of HP1a/α molecules via their *chromoshadow* domains (CSDs) (15) and the direct binding of HP1a/α dimers to H3K9me2/3 mediated by their *chromodomains* (CDs) (16). These high-affinity dimerization interactions have led the field to consider the HP1 dimer to be the biologically relevant form across homologs (17). The ability of HP1 molecules to form stable dimers also underlies a well-supported structural model for pericentromeres, whereby adjacent methylated nucleosomes are cross-linked by HP1 dimers (18, 19) – thus sequestering the underlying chromatin fiber into distinct, compact spatial compartments (henceforth referred to simply as "heterochromatin").

Yet, this relatively static description appears to be incompatible with *in vivo* observations, which have revealed a highly-dynamic exchange of HP1 molecules within heterochromatin (20). This finding mirrors the conclusions of recent studies, which have demonstrated the additional ability of various HP1 homologs to spontaneously form distinct, liquid-like condensates *in vitro* (21–23). Extensive investigations in mammals and Drosophila – based on HP1α and HP1a, respectively – have uncovered that the emergence of such higher-order oligomers is due to a complex set of low-affinity attractive forces involving both structured HP1 domains (CSD/CD) as well as multiple IDRs within the HP1a/α dimer (24, 25). This propensity for coacervation is further modulated by ionic conditions, DNA content, and post-translational modifications such as HP1α phosphorylation (21, 23), which suggests HP1-based LLPS as a potential regulatory driving force behind the segregation of methylated chromatin into heterochromatin compartments. Such a view, motivated by the demonstrated ability of HP1

to induce the robust compaction of DNA and chromatin *in vitro* (18, 26–28), would also seem consistent with the rapid kinetics of heterochromatin assembly and disassembly during the cell cycle (23, 28).

This intricate interaction network implies a complex mechanical interplay between HP1 and the chromatin polymer (23), whose effects on the formation of heterochromatin are challenging to untangle. The vast majority of models to date have hypothesized that heterochromatin compartments result solely from the capacity of HP1-like architectural proteins to carry multivalent heterotypic bonds, and hence stabilize direct, transient "bridges" between distant chromatin loci (29–31) – effectively neglecting the role of cooperative, oligomeric HP1-HP1 interactions. This putative mechanism appears to be backed by *in vivo* studies of heterochromatin condensates, whose structural properties have been reported to deviate from those typically observed *in vitro* in LLPS-driven solutions of purified proteins (32) – which has been interpreted as evidence of the prevalence of high-affinity, HP1-H3K9 "bridges" in heterochromatin assembly (11). However, this assumed dichotomy between LLPS- and "bridging"-based compartmentalization processes fails to account for the role of heterotypic, multicomponent interactions on the physics of intra-cellular phase separation (33), which may significantly affect the experimental signatures of LLPS within the crowded nuclear environment (10, 33). Furthermore, such arguments are generally based on the expected behavior of physical systems at thermodynamic equilibrium, and their practical applicability to the fundamentally out-of-equilibrium context of the cell nucleus remains unascertained (34).

Here, we comprehensively and quantitatively explore the generic physics of heterogeneous, multicomponent protein-chromatin aggregates through the lens of a minimal model of oligomeric HP1-HP1 and HP1-H3K9me2/3 interactions. We demonstrate that the key kinetic and thermodynamic features of heterochromatin formation may be reconciled with an LLPS-like mode of organization, in which chromosome structure and dynamics are driven by the coupling between fast-diffusing HP1 proteins and the constrained chromatin fiber. We further investigate how the experimental hallmarks of single-component LLPS *in vitro* may be fundamentally altered *in nucleo* by the specific affinity of HP1 for large genomic regions enriched for H3K9me2/3 (hereafter also referred to as "methylated chromatin"), both in- and out-of-equilibrium. Our theoretical predictions are corroborated by *in vivo* 4D microscopy measurements in early Drosophila embryos, and provide a general and versatile framework to interpret the endogenous behavior of a wide range of biomolecular condensates.

RESULTS

A minimal model for chromosome folding driven by self-interacting proteins

To investigate the potential interplay between the self-affinity of architectural chromatin-binding proteins such as HP1 and the large-scale organization of chromosomes, we developed a generic biophysical framework which accounts for the coupled dynamics of the chromatin polymer and self-interacting diffusible particles (see Materials & Methods and SI Methods for details). Briefly, we represent chromatin as a self-avoiding, semi-flexible chain (35) and describe protein binders via the lattice-gas model, which corresponds to an efficient molecular-level description of complex, multiphase fluids (36). The spatio-temporal evolution of the system is driven by standard polymer properties (backbone connectivity, excluded volume and bending rigidity), in conjunction with both homotypic, HP1-HP1 interactions and a heterotypic affinity of HP1 for methylated monomer sites along the chromatin chain. In this context, diffusible particles thus represent HP1 dimers with a typical hydrodynamic radius of 20 nm,

and each target monomer (referred to as a *locus*) corresponds to a contiguous chromatin region of length ~1 kbp, in which all constituent histones are assumed to bear the H3K9me2/3 post-translational mark.

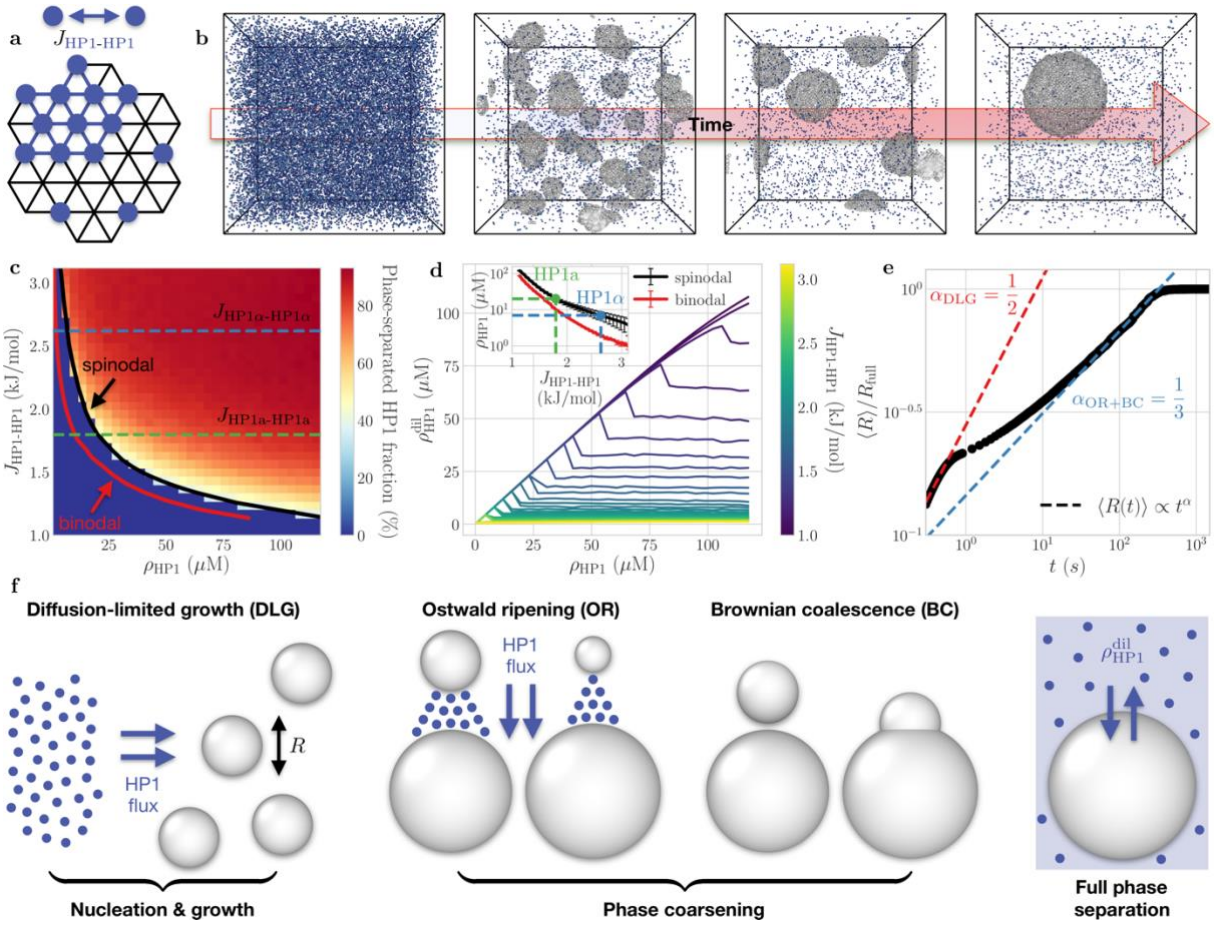

Fig. 1: Lattice-gas model (LGM) recapitulates key features of single-component LLPS. (a) Sketch of the LGM of HP1-based phase separation driven by homotypic interactions $J_{HP1-HP1}$ between proximal HP1 dimers (blue beads). (b) Typical kinetic pathway of the simulations, starting from a well-mixed, homogeneous initial state, for a set of parameters $\rho_{HP1} \cong 8\ \mu M$, $J_{HP1-HP1} \cong 2.6\ kJ/mol$ located within the two-phase coexistence region (see Movie S1). Condensed HP1 dimers are colored in grey. (c) Equilibrium phase diagram of the LGM as a function of HP1 density ρ_{HP1} and homotypic affinity $J_{HP1-HP1}$. Spontaneous demixing occurs above the spinodal line (reddish area). Dashed lines denote effective affinities inferred for HP1α (blue) and HP1a (green), respectively (see text). (d) Background HP1 density ρ^{dil}_{HP1} in the dilute phase as a function of total HP1 level ρ_{HP1}. Each line corresponds to a fixed value of $J_{HP1-HP1}$. Concentration buffering in the two-phase region manifests as a plateau in ρ^{dil}_{HP1}. Inset: Computed spinodal and binodal lines. Error bars represent standard deviations. (e) Kinetics of LLPS equilibration illustrated by the time evolution of the average condensate radius $\langle R \rangle$, normalized by its maximal value R_{full} at full phase-separation. Note the transition from rapid, diffusion-limited growth in the early nucleation regime to slower coarsening dominated by Ostwald ripening and Brownian coalescence at later stages. Simulation parameters are as in (b). (f) Standard LLPS equilibration mechanisms reproduced by the LGM.

The lattice-gas model recapitulates *in vitro* features of HP1-based LLPS

In order to critically assess the ability of the model to reproduce the main kinetic and equilibrium properties of classical, single-component LLPS, we first performed a set of simulations involving pure HP1 dimers in the absence of the chromatin scaffold (Figs.1a-b). For this purpose, we systematically varied the total HP1 concentration ρ_{HP1} and self-affinity $J_{HP1-HP1}$ between HP1-dimers starting from a well-mixed, single-phase configuration, and monitored both the time evolution and resulting steady state of the system (Fig.1b). We find

that the critical density above which coacervation occurs is a steep function of $J_{HP1-HP1}$, and decreases monotonously from $\rho_{HP1}^{crit} \cong 100\ \mu M$ to $\rho_{HP1}^{crit} < 1\ \mu M$ upon increasing $J_{HP1-HP1}$ in the range $[1\ kJ/mol, 3\ kJ/mol]$ (Fig.1c). This threshold for spontaneous phase separation is known as the *spinodal* concentration, which marks the upper limit of metastability of the single-phase region (Fig.1c, black curve). The spinodal differs from the *binodal* density (ρ_{HP1}^{dil}) of proteins observed in the dilute phase after the formation of phase-separated droplets (Fig.1c, red curve and Fig.1d) (37). This discrepancy between binodal and spinodal is found to be particularly marked for HP1-HP1 affinities $J_{HP1-HP1} \gg J_{crit}$ far above the theoretical critical point $J_{crit} \cong 0.8\ kJ/mol$ of the lattice-gas model, which corresponds to the minimal interaction strength below which HP1 dimers are incapable of spontaneous phase separation at all densities (Figs.1c-d, see Materials & Methods). Thus, although the biological literature often conflates notions of binodal and spinodal under the somewhat-ambiguous term of "saturation concentration" (7), we emphasize the general need for their distinction in quantitative studies of LLPS – specifically when mapping these critical densities to those measured *in vitro*.

Building on these considerations, to parametrize HP1-HP1 interactions, we make use of previous *in vitro* investigations of phase separation for purified HP1α and HP1a proteins in physiological buffer conditions (21, 23, 32). It is worth noting that such experiments commonly rely on the half-saturation concentration obtained from turbidity assays as a proxy for the critical (spinodal) density (ρ_{HP1}^{crit}) marking the emergence of LLPS, starting from a dilute, single-phase system. However, the quantitative link between turbidity levels and the degree of phase separation is generally unclear (38). Here, we instead identify ρ_{HP1}^{crit} as the HP1 concentration at the onset of turbidity, which may more meaningfully pinpoint the initial formation of phase-separated foci within the sample (see SI Methods). Thus, we set $\rho_{HP1\alpha}^{crit} \cong 7\ \mu M$ for mouse HP1α (23, 32), and $\rho_{HP1a}^{crit} \cong 20\ \mu M$ for Drosophila HP1a (22). Based on the computed phase diagram, the associated magnitudes of the effective inter-dimer binding affinity then read as $J_{HP1\alpha-HP1\alpha} \cong 2.6\ kJ/mol$ and $J_{HP1a-HP1a} \cong 1.8\ kJ/mol$, respectively (Figs.1c-d). These values are characteristic of weak, reversible inter-protein interactions (9, 39), and are thus consistent with an LLPS-like mode of organization. The resulting surface tension $\gamma_{HP1} \cong 10\ \mu N/m$ of the foci (Fig.S1a) is further found to be comparable in magnitude to recent *in vivo* measurements for nuclear liquid condensates (40).

The LLPS kinetics of pure HP1 predicted by the model are found to display a marked transition from a nucleation-and-growth stage at short times ($t \lesssim 1\ s$) to a coarsening behavior at longer times ($t \gtrsim 1\ s$), in agreement with classical theories of phase separation dynamics (37). The initial nucleation of HP1 foci emerges from local fluctuations of the HP1 density within the supersaturated background phase, leading to the formation of discrete seeds around which additional HP1 dimers may accumulate (Figs.1b-c). This process, known as diffusion-limited growth, is associated with rapid expansion kinetics of the mean focus size $\langle R(t) \rangle \propto t^{1/2}$ (Fig.1e) (37), constrained by the diffusion rate of individual proteins within the bulk fluid. At later time points, we observe a shift to the so-called coarsening regime, which describes the subsequent maturation and growth of an increasingly-low number of large HP1 droplets at the expense of the smaller foci. These larger condensates can form either via local collision events driven by the stochastic diffusion of proximal foci, referred to as Brownian coalescence (BC), or via non-local, transient protein "evaporation" and recondensation effects through the background phase, known as Ostwald ripening (OR) (Fig.1f) (37). These two coarsening mechanisms are associated with a slower growth exponent $\langle R(t) \rangle \propto t^{1/3}$ (Fig.1e) (37), and do not incur a net change in the bulk concentration ρ_{HP1}^{dil} of HP1 within the dilute, background

fluid. Although both evaporation and coalescence events may be observed in our simulations (Fig.1b), OR generally constitutes the dominant coarsening process in our framework – as expected from classical Cahn-Hilliard-Cook dynamics at the low protein volume fractions considered here (37) (see Materials & Methods).

Finally, upon reaching thermodynamic equilibrium, increasing the total HP1 content ρ_{HP1} is found to induce a swelling of the single, fully phase-separated condensate (Fig.1b), while the HP1 level ρ_{HP1}^{dil} outside the focus similarly remains fixed (Fig.1d). This effect, commonly known as *concentration buffering*, constitutes another hallmark of single-component LLPS (10, 41), and more formally signifies that the binodal concentration of the dilute phase is in this case independent of the total concentration of HP1 in the system (33).

Altogether, these results evidence the capacity of the model to recapitulate the salient features of classical LLPS both in and out of equilibrium, and establish the lattice-gas model as a suitable minimal description of liquid condensate formation in purified protein assays.

HP1-H3K9me2/3 affinity governs LLPS thermodynamics *in nucleo*

Having in hand a quantitative minimal model of HP1 dimer-dimer homotypic interactions, we proceeded to investigate how the formation of HP1 condensates *in vivo* may be impacted by the heterotypic affinity of HP1 proteins for H3K9me2/3-enriched loci within the chromatin polymer (Fig.2a), and to probe the potential effects of HP1-based LLPS on the structure and dynamics of heterochromatin compartments. To that end, we consider as a first test case a simplified representation of mouse chromosome 19 ($60\ Mbp$) featuring a unique, 10 Mbp-long H3K9me2/3 telocentric domain (Fig.2b), in the presence of HP1α ($J_{HP1\alpha-HP1\alpha} \cong 2.6\,kJ/mol$). We report in Fig.2d that the addition of this methylated chromatin domain considerably lowers the spinodal concentration at which HP1 foci spontaneously appear, and may thus induce the formation of HP1 condensates at intra-nuclear HP1 levels far below the critical *in vitro* concentration $\rho_{HP1\alpha}^{crit} \cong 7\ \mu M$ required for purified HP1α proteins (Figs.1c,2d). This effect is found to be increasingly pronounced upon raising the heterotypic affinity $J_{HP1-H3K9}$ in the range $[0.1\,kJ/mol\,, 0.6\,kJ/mol]$, consistent with the typical magnitude of the HP1-H3K9 binding energy suggested by previous computational studies (30). Coincidentally, although the HP1-H3K9 coupling is associated with a rise in the effective droplet surface tension (Fig.S1b), we find that the critical radius R_{crit} of the smallest thermodynamically-stable HP1-heterochromatin foci is also significantly reduced upon increasing $J_{HP1-H3K9}$ (Fig.2f). Both observations can be attributed to the preferential binding of HP1 onto the methylated chromatin substrate, which promotes phase separation by facilitating focus nucleation, and partially offsets the higher interfacial energy costs associated with smaller droplets.

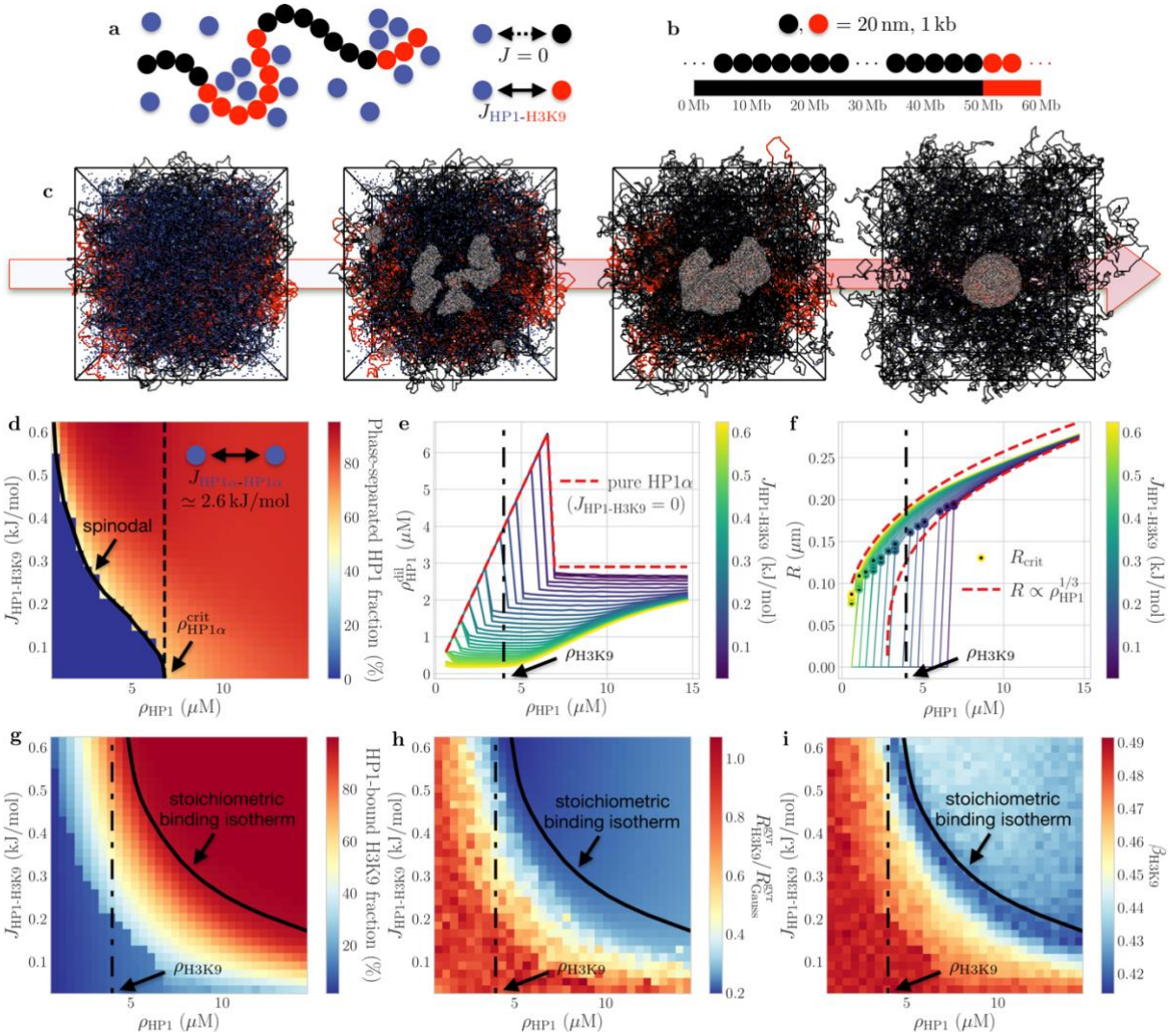

Fig. 2: HP1-H3K9me2/3 coupling affects LLPS thermodynamics. (a) Sketch of the combined HP1-chromatin simulation scheme. Self-interacting HP1α dimers ($J_{HP1-HP1} \cong 2.6\ kJ/mol$ in blue) now exhibit an additional affinity for vicinal, H3K9-methylated loci (in red) with specific binding energy $J_{HP1-H3K9}$. (b) Idealized telocentric chromosome model, with length and methylation profiles mimicking the approximate size and pericentromeric heterochromatin content of mouse chromosome 19 (42, 43). (c) Typical kinetic pathway of the simulations ($\rho_{HP1} \cong 8\ \mu M$, $J_{HP1-H3K9} \cong 0.5\ kJ/mol$), displaying rapid equilibration towards a fully phase-separated state featuring a single heterochromatin compartment (see Movie S2). (d) Equilibrium phase diagram of HP1α in presence of chromatin. HP1-H3K9 interactions may lead to spontaneous phase separation at HP1 concentrations far below the *in vitro* threshold $\rho^{crit}_{HP1\alpha}$(dashed line). (e) Dependence of the background (nucleoplasmic) HP1 level ρ^{dil}_{HP1} on the overall nuclear HP1 density ρ_{HP1} at various fixed $J_{HP1-H3K9}$. The dashed line (red) denotes values computed for pure HP1α dimers (Fig.1d), and the dash-dotted line (black) marks the nuclear methylated chromatin level ρ_{H3K9}. (f) Same as (e) for the equilibrium size R of HP1-dense foci. Dashed lines indicate the growth behavior expected of a concentration-buffered system based on the lever rule in the limits of high and low $J_{HP1-H3K9}$ (see SI Methods). R_{crit} denotes the radius of the smallest stable foci observed at each value of $J_{HP1-H3K9}$. (g) Fraction of H3K9me2/3 monomers bound to at least one HP1 dimer. The stoichiometric binding isotherm is defined as the minimal HP1 density at which this fraction reaches 100%. (h) Radius of gyration R^{gyr}_{H3K9} of the heterochromatin domain, normalized by the expected value R^{gyr}_{Gauss} for a non-interacting, Gaussian coil. Maximal heterochromatin compaction (i.e., minimal R^{gyr}_{H3K9}) is achieved along the isotherm. (i) Diffusion exponent β_{H3K9} of methylated loci ($MSD_{H3K9}(\Delta t) \sim D_{H3K9}\Delta t^{\beta_{H3K9}}$), evidencing their strongly-subdiffusive motion ($\beta_{H3K9} < 1$).

Furthermore, in contrast to the pure HP1 system, the potential concentration buffering behavior in the two-phase regime is now dependent on the system composition (Fig.2e). For moderate-to-high affinity strengths $J_{HP1-H3K9}$, we observe that the HP1 density ρ^{dil}_{HP1} in the dilute,

nucleoplasmic phase remains almost constant for low HP1 expression levels ρ_{HP1}, then increases with ρ_{HP1} at intermediate HP1 densities, and only approaches its *in vitro* (binodal) plateau value (Figs.2e, red line and 1e, inset) in the limit of high concentrations. In both the low and high density regimes, the volume $V \propto R^3$of HP1-dense foci grows roughly linearly with ρ_{HP1}, consistent with standard concentration buffering (Fig.2f, see SI Methods). This can be interpreted as a stoichiometric effect, resulting from the finite valency of H3K9me2/3 loci. Indeed, by inspecting the HP1-H3K9 binding landscape (Fig.2g), we find that the minimal HP1 concentration at which each H3K9me2/3 locus is in contact with at least one HP1 dimer depends on $J_{HP1-H3K9}$ (Fig.2g, black line). This so-called *stoichiometric binding isotherm* gradually converges towards the volumic density ρ_{H3K9} of methylated chromatin in the limit of strong affinities – in which most of the HP1 dimers are wetting H3K9me2/3 sites, and the population of free dimers is negligible ($\rho_{HP1}^{dil} << \rho_{HP1}$) (Fig.2e). For HP1 densities below the isothermal value, the system is in a regime of droplet growth driven by HP1-H3K9 binding events, and eventually reaches saturation at the isotherm (Fig.2e). Beyond this point, additional dimers chiefly diffuse into the nucleoplasmic background phase, as further swelling of the droplets does not incur any gains in HP1-H3K9 contacts. Thus, one generally obtains a sublinear growth of the focus volume V with increasing ρ_{HP1} (Fig.2f), and only recovers the usual buffering behavior in the limit of wide HP1 excess ($\rho_{HP1} \gg \rho_{H3K9}$) – in which HP1-H3K9me2/3 coupling becomes statistically irrelevant, and is superseded by HP1-HP1 homotypic interactions (Figs.2e-f).

The formation of HP1-heterochromatin condensates is further found to drive the partial or total collapse of the encapsulated methylated chromatin (Fig.2h). This structural transition starts when roughly 20-30% of the H3K9me2/3 loci are covered by HP1 dimers, and is also associated with a dynamical crossover, whereby the methylated chromatin diffusion constant is reduced by roughly fivefold (Fig.S3f) and the diffusion exponent goes from 0.5 – consistent with the viscoelastic dynamics of a dilute, unconstrained polymer – down to ~ 0.4, characterizing the slower motion of a dense, globular chain (Fig.2i) (44). Interestingly, the stoichiometric binding region coincides with a maximal impact on the compaction and mobility of the methylated chromatin region (Figs.2h,i and S2h), which results from the full encapsulation of all H3K9me2/3 loci within a HP1 focus of minimal volume – and thus leads to the maximal degree of heterochromatin packaging.

Together, these conclusions demonstrate the ability of HP1-based LLPS, coupled with the specific affinity of HP1 for methylated chromatin regions, to mediate the stable formation of condensed heterochromatin compartments at endogenous levels far below the critical phase separation concentration observed in purified *in vitro* assays. This result also highlights the limitations of intra-cellular perturbation experiments based on ectopic protein over- or under-expression in investigations of LLPS *in vivo* (32), whose interpretation in terms of buffering behavior generally requires a careful quantitative analysis of the endogenous concentrations of all the interaction partners involved (33).

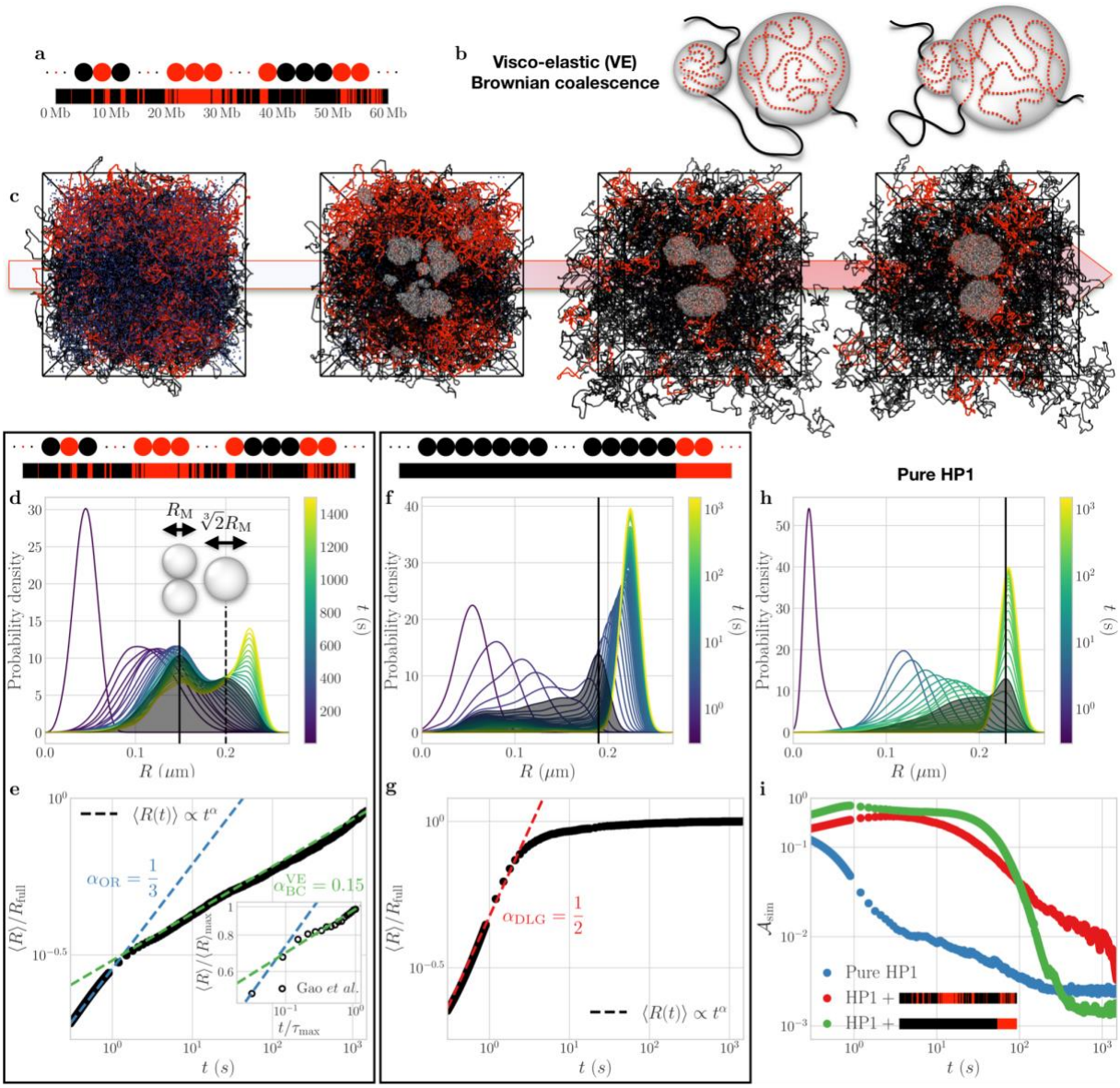

Fig. 3: H3K9me2/3 distribution and chromatin mechanics govern LLPS kinetics. (a) Representation of human chromosome 19, with H3K9me2/3 patterns inferred from ChIP sequencing data (see SI Methods). (b) Illustration of the viscoelastic (VE) Brownian coalescence process. Anomalously-slow equilibration arises from the dynamical coupling between fast-diffusing HP1 proteins and the more constrained motion of the methylated chromatin scaffold. (c) Typical kinetic pathway of the simulations, evidencing the OR evaporation of small foci at short times and the VE coalescence of larger foci at longer times (see Movie S3). (d) Time evolution of droplet size populations for the HP1+human chromosome 19 system, obtained by kernel density estimation of the probability distribution function of focus radii R. The prevalence of VE coalescence at later stages manifests via the emergence of a growing secondary peak in the distributions, which proceeds from discrete collision events. (e) Associated evolution kinetics of the mean droplet radius $\langle R\rangle$, which reveals the transition from OR-dominated ($t \lesssim 1\ s$) to anomalously-slow VE coarsening ($t \gtrsim 1\ s$). Inset: Experimental data from Ref. (45), obtained from the mean fluorescence intensity of engineered HP1 puncta (see SI Methods). (f), (g) Same as (d), (e) in the case of an idealized telocentric chromosome. Phase separation is considerably accelerated by the cooperative binding of HP1 onto the single methylated region. (h) Same as (d) for pure HP1α dimers (c.f. Fig.1e). Phase coarsening is now dominated by Ostwald ripening, which yields left-skewed, unimodal distributions consistent with Lifshitz-Slyozov-Wagner statistics (37). (i) Time evolution of the focus anisotropy $\mathcal{A}_{sim}$, such that $\mathcal{A}_{sim} = 0$ for ideal spheres and $\mathcal{A}_{sim} \to 1$ for elongated droplet shapes (see SI Methods). Simulation parameters in (c)-(i) are as in Figs.1b,2c.

H3K9me2/3 distribution and chromosome mechanics regulate LLPS kinetics

The coupled evolution dynamics of the HP1-chromatin system studied in Fig.2 irreversibly leads to rapid relaxation towards a fully phase-separated state, characterized by the complete segregation of methylated chromatin into a single, large focus encapsulated within a unique HP1 liquid droplet (Fig.2c, right). The phase separation kinetics predicted by the model in this case reveal a quick equilibration of the mean focus size over a typical timescale $t \lesssim 10\ s$ with a growth exponent $\langle R(t) \rangle \propto t^{1/2}$, consistent with nucleation-driven diffusion-limited growth (Fig.3g). We attribute this effect to the cooperative binding of HP1 onto the contiguous methylated chromatin domain, which leads to the strong co-localization of droplet nucleation sites within the same, H3K9me2/3-dense nuclear region (Fig.2c, left) – and thus mostly obviates the slower, large-scale rearrangements associated with OR and BC for homogeneously-distributed, fluctuation-induced initial seeds (Figs.1b-c). However, this mode of organization may contrast with the multiplicity of spatially-distinct heterochromatin compartments per chromosome commonly observed in higher eukaryotes (46), which may be stably maintained across multiple cell cycles in conventional cycling nuclei (43). Such complex, heterogeneous domain patterns constitute a hallmark feature of 3D chromosome structure (47), and are traditionally interpreted in terms of the *microphase separation* process undergone by block copolymers in the presence of affinity interactions involving distinct epigenomic regions (48).

To investigate whether such long-lived, microphase-separated compartments may be physically reconciled with a LLPS-based mechanism of chromatin folding, we introduced as a second test case a chromosome model featuring multiple methylated domains of disparate sizes, representative of chromosome 19 in human fibroblasts (Fig.3a, see SI Methods). We find that this heterogeneous distribution of H3K9me2/3 along the chromatin polymer gives rise to drastically-slower equilibration kinetics, whereby HP1 dimers stochastically aggregate across multiple separate methylated chromatin regions (Fig.3c). These competing nucleation sites then gradually mature into a number of distinct, spherical liquid foci, which may remain metastable over timescales $t \gg 30\ min$ well beyond the total simulation time (Figs.3c-e). This partial phase coarsening process is characterized by the rapid evaporation of smaller foci at short times $t < 1\ s$ (Fig.3c), associated with a mean growth exponent $\langle R(t) \rangle \propto t^{1/3}$ consistent with classical OR (Fig.3e). Such evaporation events are however found to be strongly suppressed at longer timescales, over which focus growth is instead governed by an abnormally-slow growth exponent $\langle R(t) \rangle \propto t^{0.15}$ (Fig.3e).

Similar anomalous coarsening dynamics have been recently reported for engineered intra-nuclear protein condensates, and were ascribed to the coupling of droplet motion with the viscoelastic (VE) diffusion kinetics of the underlying chromatin network (49–51). Indeed, the strong colocalization of H3K9me2/3 loci within liquid-like HP1 foci (Figs.2c,g) imposes that condensate displacements correlate with the collective diffusion of the encapsulated methylated chromatin regions (Fig.3b). Hence, the diffusion exponent β of individual foci necessarily matches that $\beta_{H3K9} \cong 0.45$ associated with the sub-diffusive motion of compact heterochromatin domains (Fig.2i) (44). In this case, one may show (49) that the theoretical coarsening dynamics associated with BC, driven by the mutual diffusion of HP1 droplets, simply scale as $\langle R(t) \rangle \propto t^{\beta/3}$ – from which one recovers the usual growth exponent $\alpha_{BC} = 1/3$ if the foci exhibit regular Brownian motion as in standard LLPS, unhindered by the chromatin scaffold ($\beta = 1$, Figs.1e-f). The measured scaling behavior $\alpha_{BC}^{VE} \cong 0.15$ (Fig.3e) is thus consistent with these anomalously-slow, viscoelastic coalescence events coupled to the inhibition of OR, which we attribute to the effective "trapping" of H3K9me2/3 domains within the nucleated HP1 droplets (52).

These conclusions are corroborated by a more detailed analysis of the time evolution of the associated droplet size distributions (Fig.3d,f,h). In the case of pure HP1, for which OR constitutes the primary coarsening mechanism (see above), the corresponding focus population displays a characteristic unimodal, left-skewed transient shape at intermediary times $1\ s < t < 300\ s$ (Fig.3h). These results are consistent with the classical Lifshitz-Slyozov-Wagner theory (37), in which the left long tail of the distribution corresponds to a polydisperse population of small droplets undergoing continuous evaporation. These population dynamics are qualitatively similar to those observed in the presence of a single, large centromeric heterochromatin region (Fig.3f) – which may be imputed to the rapid nucleation of HP1 foci onto the homogeneously-methylated chromatin substrate (53). Conversely, in the case of a highly-dispersed pattern of H3K9me2/3 marks (Fig.3d), we find that this left-skewed long tail is noticeably less pronounced. The droplet size distribution then displays a growing secondary peak centered around radii $R \cong \sqrt[3]{2}\,R_M$ significantly larger than the most-probable value R_M at the primary peak (Fig.3d). We therefore attribute this transient, bimodal behavior to the prevalence of discrete coalescence events involving separate methylated chromatin domains, leading to the sudden emergence of a distinct population whose volume $V \propto R^3$ matches twice that of the dominant droplet size R_M.

Remarkably, a recent *in vivo* study based on CRISPR-engineered HP1 targeted to ectopic chromatin binding sites (45) revealed that the assembly kinetics of HP1 foci at their distributed target loci follow a similar transition from a $\alpha \cong 1/3$ short-time exponent to a slower growth regime with $\alpha \cong 0.15$ at longer times (Fig.3e, inset). These findings suggest that the coarsening behavior reported in Fig.3e generally arises from the interplay between LLPS and chromosome mechanics in the presence of multiple, competing genomic binding regions. Thus, our results suggest that the microphase separation of heterochromatin into long-lived, coexisting nuclear compartments could be simply attributed to anomalously-slow equilibration kinetics originating from the dynamical asymmetry between fast-diffusing HP1 proteins and the slow, viscoelastic chromatin scaffold.

Heterochromatin establishment kinetics govern focus morphology

In a wild-type context, an additional factor relevant to the coupling between chromatin and HP1-based LLPS *in nucleo* may be the constant out-of-equilibrium dynamics of the methylated chromatin landscape, which may arise either from the establishment of H3K9me2/3 marks during embryogenesis and differentiation, or from their maintenance after replication (13). To address the effects of H3K9me2/3 establishment on the assembly kinetics of HP1 condensates, we investigated the formation of heterochromatin compartments during early fly embryogenesis. In Drosophila, most of the heterochromatin is localized at the pericentromeric regions, forming large, ~20-45 Mbp-wide, contiguous H3K9me2/3 domains encompassing almost 30% of the genome (55). During embryogenesis, the majority of methylated chromatin is established during nuclear cycles 11 through 14 (NC11-14), concomitant with the successive formation and dissolution of increasingly-large spatial HP1-heterochromatin compartments (22).

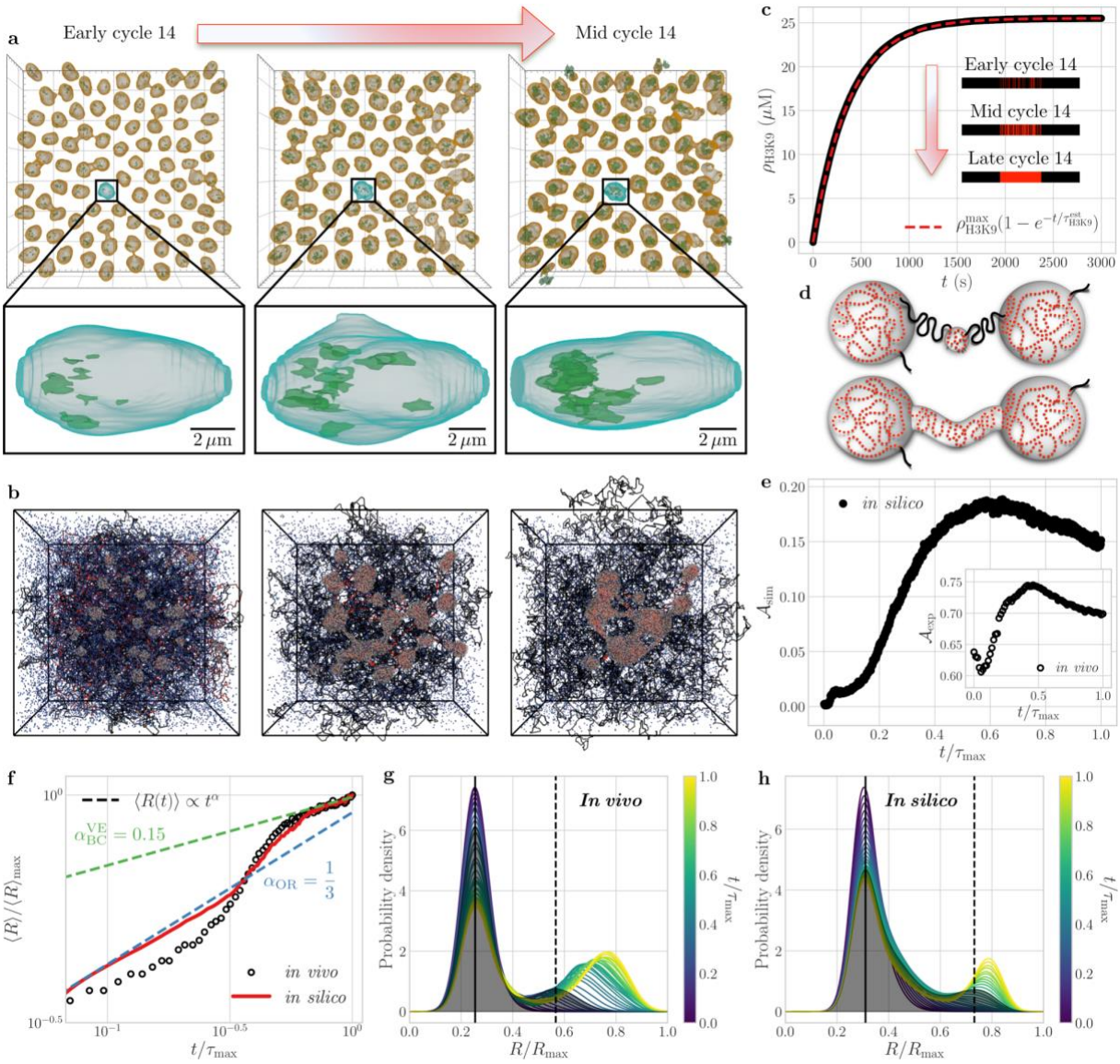

Fig. 4: Role of H3K9me2/3 establishment kinetics: The case of Drosophila embryogenesis. (a) Surface reconstructions of HP1a foci within Drosophila nuclei during NC14. Time points shown are 5, 10, & 15 minutes from NC13 mitotic exit. (b) Typical kinetic pathway of the simulations over the first $\sim 1000\ s$ of Drosophila NC14, displaying increasingly aspherical, branched HP1 focus morphologies (see Movie S4). Simulation parameters are as in Fig.2c in presence of HP1a ($J_{HP1-HP1} \cong 1.8\ kJ/mol$). (c) Modeled H3K9me2/3 establishment dynamics, with uniform methylation rate $\tau^{est}_{H3K9} \cong 5\ min$ chosen to approximate the reported evolution of NC14 H3K9me2/3 levels (54). (d) Illustration of the non-local focus bridging mechanism induced by late-stage methylation events. (e) Time evolution of the focus anisotropy in both simulation ($\mathcal{A}_{sim}$) and *in vivo* microscopy data ($\mathcal{A}_{exp}$) (see SI Methods). Gradual relaxation towards spherical morphologies ($\mathcal{A} = 0$) is observed for $t \gtrsim 1000\ s$, for which near-total H3K9me2/3 establishment has been achieved (Fig.4c). (f) Same as (e) for the mean droplet radius $\langle R \rangle$, evidencing the transition from evaporation-driven OR ($\alpha \cong \frac{1}{3}$) to coalescence-dominated VE coarsening behavior ($\alpha \cong 0.15$) as the cell cycle progresses (c.f. Fig.3e). (g), (h) Time evolution of the associated droplet size populations *in vivo* (g) and *in silico* (h). The persistent primary peak at small R reflects the occurrence of late-stage nucleation events, while the secondary peak at large R denotes the growing population of increasingly-large foci, which may arise from both bridging-induced (Fig.4d) and Brownian coalescence (Fig.3b). $R^{in\ vivo}_{max} \cong 1.7\ \mu m$ (g) and $R^{in\ silico}_{max} \cong 0.4\ \mu m$ (h).

We thus introduced a minimal description of H3K9me2/3 establishment in which, starting from a fully unmethylated initial state, each pericentromeric locus may stochastically acquire the H3K9me2/3 mark with a fixed methylation rate τ^{est}_{H3K9}. Focusing on the case of *D. melanogaster*

chromosome 2 (48.8 Mbp, Fig.4b), we parameterized intra-nuclear HP1a and H3K9me2/3 concentrations based on mass spectrometry analysis of *D. melanogaster* embryos (56), and set $\tau_{H3K9}^{est} \cong 5$ minutes to mimic the typical evolution of methylated chromatin levels reported over the course of Drosophila NC14 (54, 57, 58) (Fig.4c, see SI Methods). Furthermore, in order to assess the biological relevance of our findings, we simultaneously examined the spatio-temporal dynamics of GFP-HP1a puncta across NC14 in live Drosophila embryos by means of 4D confocal microscopy (Fig.4a, see Materials & Methods), and jointly monitored the time evolution of condensate sizes and morphologies to directly juxtapose model predictions against experimental measurements over the first $\tau_{max} \cong 40$ minutes of NC14.

Our simulations predict that the growth exponent α of the foci displays a crossover from $\alpha \cong 1/3$ at short times to $\alpha \cong 0.15$ at later stages (Fig.4f), qualitatively similar to that obtained in the case of multiple competing, human-chromosome-19-like heterochromatin domains (Fig.3e). However, this slower, competitive mode of phase separation contrasts with the faster, cooperative LLPS kinetics ($\alpha \cong 1/2$) expected for the steady-state distribution of H3K9me2/3, which consists in one contiguous block of methylated chromatin (Fig.4c, late NC14) – much like our telocentric mouse-like chromosome model (Fig.3g). We attribute this anomalously-slow equilibration process to the dynamic propagation of H3K9me2/3, which may lead to transient stochastic patterns featuring multiple, distinct H3K9me2/3-enriched regions as methylation progresses (Fig.4c, early/mid NC14) — which may in turn act as competing seeds for the nucleation of HP1 condensates. The resulting shift in the focus growth exponent from $\alpha \cong 1/3$ to $\alpha \cong 0.15$ is associated with a transition regime around $t \sim 10^{-0.5}\tau_{max} \cong 15\ min$ (Fig.4f), during which coarsening is mainly driven by non-local percolation events induced by the formation of bridges between distal HP1 foci (Figs.4b,d, see below). These predictions are fully corroborated by *in vivo* data analysis (Figs.4a,f), and suggest that the overall assembly kinetics of HP1-dense compartments in NC14 are chiefly limited by the intrinsic coarsening behavior of the coupled HP1-chromatin system, rather than by the detailed biochemical mechanisms involved in heterochromatin establishment.

Remarkably, the maturation of these HP1-heterochromatin foci is found to be associated with an increasing loss of sphericity during the establishment of the methylated pericentromeric domain, which is evidenced in both model and experiment by a sharp rise in the mean focus anisotropy $\mathcal{A}$ during the first 20-30 min of NC14 (Fig.4e, see SI Methods) (22). This behavior markedly differs from that expected for simple fluids, in which surface tension generally drives droplets to adopt increasingly-round shapes ($\mathcal{A} = 0$) to minimize interfacial energy, as observed in simulations of pure HP1 (Fig.3i). It also contrasts with our model predictions for the coupled HP1-chromatin systems in the absence of H3K9me2/3 establishment dynamics, for which $\mathcal{A}$ similarly decays towards 0 after a short initial plateau (Fig.3i) — indicating a gradual convergence towards spherical morphologies after a short lag time, corresponding to the conformational relaxation time of the encapsulated methylated chromatin. Thus, the increase in anisotropy observed in our embryo simulations can be attributed to the dynamic propagation of chromatin methylation. Indeed, the creation of new H3K9me2/3-enriched regions leads to the continuous nucleation of small HP1 puncta, which may eventually percolate into bridged structures linking larger foci — associated with early-methylated chromatin domains — in a network-like fashion (Figs.4b,d). Such complex, non-convex morphologies are fully consistent with *in vivo* observations at mid-NC14 (Fig.4a), and develop as the system proceeds towards full heterochromatin establishment — at which point new nucleation events subside, and the condensates slowly relax towards their equilibrium shape (Fig.4e).
This mechanism is also evidenced by the evolution of the focus size distributions, which reveals the presence of a significant population of small droplets that persists throughout most of NC14

(Figs.4g-h), as opposed to the rapid disappearance of small puncta obtained for both pure HP1 (Fig.3h) and static methylated chromatin domains (Figs.3d,f). This population results from continuous late-stage nucleation and is gradually superseded by a distinct population of significantly-larger foci as the cell cycle progresses (Figs.4g-h), which emerges chiefly through viscoelastic BC events as one approaches full H3K9me2/3 establishment and HP1 nucleation recedes (Figs.3b,4f). Together, these observations suggest that the formation of spatially-distinct, long-lived heterochromatin compartments may be generically facilitated by H3K9me2/3 propagation, which further promotes anomalously-slow HP1 phase separation kinetics by introducing a competition between nucleated HP1 foci within individual pericentromeres. More broadly, these results illustrate how the dynamic nature of H3K9me2/3 establishment may drive the system away from equilibrium and lead to the development of increasingly aspherical, network-like HP1-heterochromatin morphologies, which can nevertheless appear to remain stable across most of the cell cycle.

DISCUSSION AND CONCLUSION

In this study we have used generic biophysical modeling to investigate how the propensity of architectural chromatin-binding proteins such as HP1 to undergo LLPS may be impacted by heterotypic, specific interactions with the chromatin fiber, and may in turn affect both chromosome structure and mobility. In particular, we demonstrate that the equilibrium and kinetic features of *in nucleo* LLPS may quantitatively and qualitatively deviate from the classical hallmarks of single-component LLPS in several key aspects (59). First, our model predicts that, *in vivo*, HP1 condensates may stably form at H3K9me2/3-enriched genomic regions at physiologically-relevant concentrations of HP1, which are significantly lower than the *in vitro* spinodal density (Fig.2d). Such "polymer-assisted condensation" (60) emerges from the *indirect* stabilization of HP1-HP1 contacts caused by the *direct* affinity interactions between HP1 and H3K9me2/3 nucleosomes. This heterogeneous nucleation process is fully consistent with other theoretical models of self-attracting, diffusing particles – like RNA Pol II or the pioneer transcription factor Kfl4 – which may also display a specific affinity for the chromatin polymer (61–63).

Second, we show that, *in vivo*, the (binodal) nucleoplasmic density of HP1 in the dilute background phase is generally not constant, but instead depends on the total HP1 level (Fig.2e). When HP1 molecules are present at sub-stoichiometric levels compared to methylated chromatin sites, nucleoplasmic HP1 is buffered at a fixed value significantly lower than that measured *in vitro*. This depletion of HP1 in the dilute phase is more pronounced for stronger HP1-H3K9me2/3 interactions. Conversely, when HP1 dimers are in excess of H3K9me2/3, we predict a sub-linear increase of nucleoplasmic levels with the global HP1 concentration, associated with an anomalously-slow growth of the heterochromatin compartment (Fig.2f). A similar increase of the nucleoplasmic concentration was recently observed in mouse embryonic fibroblast when overexpressing HP1α (32), but also in HeLa cells for several proteins like NPM1 involved in the formation of other LLPS-based condensates such as nucleoli (33). Although such stoichiometric effects are frequently attributed to compartmentalization mechanisms involving non-cooperative "bridger" proteins (see below) (1), our findings reveal that this behavior may also be displayed by protein-based liquid condensates in the presence of heterotypic interactions – in agreement with the generic properties of multicomponent LLPS (33, 64).

Third, our analysis demonstrates that, *in vivo*, the kinetics of condensate coarsening depends on the linear organization of methylated chromatin along the genome, and may significantly deviate from the standard *in vitro* behavior driven chiefly by Ostwald ripening and simple Brownian coalescence (Fig.3). Condensate formation around long contiguous H3K9me2/3 regions is anomalously-fast (Fig.3g), and may allow the rapid recompaction of large methylated domains such as pericentromeres in late mitosis/early interphase, after the disassembly of HP1-heterochromatin foci during mitotic prophase (22). On the contrary, the coarsening of scattered (Fig.3e) or establishing (Fig.4f) H3K9me2/3 domains is anomalously-slow and dominated by visco-elastic Brownian coalescence. Interestingly, such inhibited equilibration kinetics corroborate *in vivo* measurements for HP1 (45) and FUS (49) proteins as well as *in silico* studies of nucleolus formation (51), and appear to generically characterize liquid droplets embedded in a polymer network – regardless of whether the heterotypic interactions with chromatin are attractive (51) or repulsive (49, 65). In a developmental context, these slow coalescence dynamics may further explain why, in cycling cells, all methylated chromatin regions – initially spatially-dispersed after mitosis – generally do not colocalize into one single macro-phase, but rather form several meta-stable micro-compartments, whose fusion may be too slow to be achieved within one cell cycle (66). Our prediction is that post-replicative cells may exhibit fewer and larger heterochromatin condensates, as has already been reported in oncogene-induced senescent fibroblasts (66) and in mouse rod photoreceptors (43). Together, these conclusions evidence the limitations of interpreting potential intra-cellular observations of endogenous LLPS based on simple comparisons to the thermodynamic and kinetic properties of single-component LLPS.

In this context, it is enlightening to compare our results to those of previous "bridger"-based descriptions of compartment formation, such as the string-and-binders-switch model (32, 34, 65). Such approaches, which neglect the effects of HP1-HP1 oligomeric interactions (Fig.S2a), are found to display many quantitative and qualitative differences with the behavior of our model (Figs.S2-S3). For instance, in the "bridger" model, the variations in nucleoplasmic HP1 density exhibit the same qualitative trends as in our case (Fig.S2d), but the increase with HP1 concentration in the regime of stoichiometric excess is significantly more pronounced (Fig.2e). Another notable distinction lies in the interplay between HP1 and heterochromatin condensation. In the "bridger" model, both processes are tightly coupled and occur near-simultaneously (Figs.S2c,S3a), with a strong theta-collapse of the long H3K9me2/3 domains leading to high polymer compaction (Fig.S3a) as well as a dramatic reduction of the chromatin mobility (Fig.S3c). Conversely, we observe that the nucleation of HP1 condensates at H3K9me2/3 regions may occur at much lower densities than those at which maximal heterochromatin compaction is achieved (Figs.2d,h), which gives rise to a more diffuse transition between the dilute coiled and dense globular states. Furthermore, the chromatin configurations predicted by our model are generally less compact (~twofold, Figs.S3a,d) and more dynamic (~fivefold, Figs.S3c,f) than in the "bridger" model.

Therefore, our results demonstrate that the composition dependence of nucleoplasmic HP1 levels and the presence of a switch-like coil-to-globule transition, which have been previously presented as irreconcilable with LLPS behavior (32), are actually compatible with both "bridger"- and LLPS-based mechanisms of chromatin condensation. Furthermore, it is worth pointing out that these two processes are not necessarily mutually-exclusive. Indeed, the biophysical properties of condensates are known to evolve over the course of the cell cycle and cellular differentiation, displaying liquid-like properties during initial establishment that transition into more static, gel-like material states consistent with maintenance (22, 67). This crossover could reflect the differential regulation of HP1 homotypic and heterotypic affinities

by various post-translational modifications (68), as well as potential chromatin cross-linking by HP1 binding partners (69), which could conceivably enable endogeneous HP1 to exhibit a full spectrum of *in vivo* behaviors in-between those of the "bridger" and self-interacting binder models. In biological situations like early embryogenesis, where heterochromatin needs to be mobile and (re)organized on a large scale during the initial establishment of the condensate, dynamic, LLPS-like properties may be more functionally desirable. However, in more differentiated cells, a constrained, "bridger"-like mode of heterochromatin segregation may be more advantageous to ensure the higher compaction and complete silencing of methylated genomic regions, or to provide specific mechanical or optical properties to the nucleus (70, 71). Indeed, HP1 mobility inside heterochromatin has been shown to be tightly regulated, and to gradually decrease as embryogenesis progresses (22).

In addition to the magnitude of HP1-associated affinities, our analysis of early fly embryogenesis shows that the spatio-temporal dynamics of HP1 condensates also depends on the time evolution of the H3K9me2/3 distribution (Fig.4). In our work, to focus on HP1 condensate coarsening, we considered simplified, stochastic kinetics of H3K9me2/3 domain formation (Fig.4c). More realistically, the establishment of H3K9me2/3 domains may rely on a feed-forward spreading mechanism, whereby lysine methyltransferases (KMTs) like Su(var)3-9, SetDb1 or G9a propagate methylation marks from recruitment sites via auto-catalytic reader-writer processes (13, 72, 73). As the nuclear concentration of KMTs is usually low (56), the rapid establishment of heterochromatin domains during development would require an efficient long-range spreading activity for KMTs (74). Therefore, the spatial organization of chromatin around KMT nucleation sites may play an important role in the regulation of such activity (75). The recruitment of HP1 by nascent H3K9me2/3 regions, and the subsequent 3D compaction of methylated chromatin, could facilitate the long-range spreading of methylation marks through a positive feedback loop based on the interplay between HP1 recruitment and chromatin compaction, which may accelerate the establishment of epigenetic patterns (76–78). While this amplification loop may be essential to facilitate the spreading of heterochromatin, the very good agreement between our predictions and experiments (Figs.4e-h) indicates that the large-scale coarsening dynamics of HP1 condensates are not strongly limited by the underlying kinetics of H3K9me2/3 establishment. Instead, our results would suggest the aspherical morphology of such condensates as a generic experimental signature of the out-of-equilibrium character of the epigenetic landscape (Figs.4d-e).

To conclude, we have developed a generic quantitative framework to investigate the LLPS of architectural chromatin-binding proteins *in nucleo*, and contextualized our investigations to the formation of heterochromatin in higher eukaryotes. To perform such a systematic analysis, we however had to resort to several simplifying assumptions. First, we limited our analysis to a finite-size system consisting of a single chromosome. Our results in the case of the human (Fig.3) and Drosophila (Fig.4) nuclei suggest that the presence of other chromosomes – and thus, of other competing H3K9me2/3 regions – could add an additional layer of visco-elastic coarsening dynamics driven by inter-chromosomal diffusion kinetics. Such very slow processes (79) may generally prohibit the fusion of inter-chromosomal condensates, except in cases where the majority of H3K9me2/3 regions are co-localized post-mitosis, as in the Rabl configuration observed during fly embryogenesis (80). Second, we did not explicitly consider the dimerization thermodynamics of HP1, and did not account for the finite interaction valency of HP1 with chromatin (81, 82). These effects could possibly alter the impact of HP1 on heterochromatin compaction (63, 83), and may also affect the binodal and spinodal concentrations of HP1 *in vivo* – especially for endogenous HP1 levels close to the dimer dissociation constant. Finally, we restricted our work to a binary HP1-H3K9me2/3 system,

neglecting other interaction partners such as RNA or HP1 binding factors that may interfere with or facilitate the formation of heterochromatin, which could serve to further enhance the complexity of the corresponding multicomponent LLPS phase diagram (84, 85).

Future studies will thus have to integrate such ingredients, coupled to a more precise description of H3K9me2/3 establishment, in order to fully characterize the spatio-temporal dynamics of heterochromatin in various biological contexts – such as (e.g.) the DNA repair of methylated chromatin loci (86) – as well as to investigate the important role of HP1 in structuring non-pericentromeric regions (87, 88). Nonetheless, the examination of the transferability of our minimal model to other architectural proteins constitutes a promising avenue of research, in light of its remarkable ability to correctly capture the *in vivo* features of HP1-based heterochromatin formation. In this framework, a natural potential candidate is PRC1, which plays a crucial role in the regulation of Polycomb target genes (89) and has similarly been shown to exhibit LLPS-like properties *in vitro* (90, 91).

ACKNOWLEDGEMENTS

We are grateful to members of the Karpen and Jost labs for fruitful discussions and Geoff Fudenberg and Aurèle Piazza for a critical reading of the manuscript. Part of this work was initiated during the KITP Program: Biological Physics of Chromosomes 2020 (supported by the National Science Foundation under Grant No. NSF PHY-1748958 and NIH Grant No. R25GM067110). Work in the Jost lab is funded by Agence Nationale de la Recherche (ANR-18-CE12-0006-03; ANR-18-CE45-0022-01). The Karpen lab acknowledges National Institute of Health (R35GM139653) and Volkswagen Stiftung (98196) for funding. We thank PSMN (Pôle Scientifique de Modélisation Numérique) and CBP (Centre Blaise Pascal) of the ENS de Lyon for computing resources.

MATERIALS & METHODS

Lattice-gas model of HP1-based phase separation

Individual HP1 dimers were represented as spherical beads with effective diameter δ residing on the vertices of a face-centered cubic lattice $\mathcal{L}$ (Fig.1a). Multivalent affinity interactions between proximal dimers were described by a nearest-neighbor pair potential of depth $J_{HP1-HP1}$,

$$\mathcal{H}_{HP1-HP1} = -\frac{J_{HP1-HP1}}{2}\sum_{i\in\mathcal{L}}\sum_{j\in\mathcal{V}(i)}\sigma_i\sigma_j, \quad (1)$$

where the double sum runs over each lattice site i and its 12 connected neighbors $j \in \mathcal{V}(i)$. In Eq. (1), the occupancy number σ_i equals 1 if a dimer is present at site i and 0 otherwise, reflecting the fact that each lattice site may contain at most a single HP1 dimer. The lattice is comprised of a finite number $\mathcal{N}$ of vertices, and periodic boundary conditions were used to mimic potential cross-interactions with vicinal intra-nuclear regions.

Simulations were initialized by uniformly distributing a number $\mathcal{N}_{HP1}$ of HP1 dimers on the lattice in a random arrangement, and were evolved through standard kinetic Monte Carlo (MC) rules at fixed temperature $T = 300\ K$ (92). In this context, the critical point J_{crit} of the lattice-gas model predicted by mean-field theory reads as $J_{crit} = k_B T/3 \cong 0.8\ kJ/mol$ (36), with k_B the Boltzmann constant, which marks the dimer-dimer interaction threshold below which HP1 may not spontaneously phase separate at any concentration. Each MC step then consists of an arbitrary number N_{trial} of trial moves, in which a constituent HP1 dimer is first selected

at random, whose position on the lattice we denote by p. The particle is then displaced to a random neighboring site $q \in \mathcal{V}(p)$, with an acceptance probability provided by the Metropolis criterion associated with the Hamiltonian in Eq. (1). In the event that site q is also occupied by another HP1 dimer, we implement a particle exchange protocol between sites p and q with an acceptance probability of 1, reflecting the invariance of Eq. (1) to such molecular swap moves. These evolution rules ensure that the system emulates Cahn-Hilliard-Cook (also known as *Model B*) dynamics in the continuum limit (93), and are therefore suitable for the investigation of LLPS kinetics in the case of negligible hydrodynamic interactions (37) – an assumption consistent with the hydrodynamic screening approximation commonly used in numerical simulations of chromatin-based processes *in nucleo* (94).

In this framework, the overall molecular level ρ_{HP1} of HP1 is governed by the fraction $\mathcal{N}_{HP1}/\mathcal{N}$ of occupied lattice sites, which remains fixed over the course of the simulations, and is such that $\mathcal{N}_{HP1}/\mathcal{N} \lesssim 0.1$ for all systems considered here. Since we here mostly focus on the density regime $\rho_{HP1} \gtrsim K_d$, with $K_d \cong 1\ \mu M$ the HP1 dimer dissociation constant, we assume that the majority of HP1 is present in dimerized form, and neglect the population of free HP1 monomers as a first approximation. In this case, the molar concentration of HP1 simply reads as $\rho_{HP1} = 2\,\mathcal{N}_{HP1}/\mathcal{N} \times 1/N_A v_{site}$, with N_A the Avogadro constant and $v_{site} = \delta^3/\sqrt{2}$ the effective volume of each lattice site. We set $\delta = 20\ nm$, consistent with the approximate radius of gyration $2R_{gyr} \cong 15\ nm$ of the extended conformation of HP1α dimers (21), which has been shown to be generally prevalent in phase-separated HP1 assemblies (21, 24). R_{gyr} was estimated from the corresponding SAXS distance distribution $P(r)$ (21) via (95)

$$R_{gyr}^2 = \frac{\int_0^{r_{max}} P(r) r^2 dr}{2 \int_0^{r_{max}} P(r) dr}.$$

Polymer model of chromatin

Chromatin was described as a self-avoiding, semi-flexible polymer chain comprised of $\mathcal{N}_{chr}$ monomers, represented as spherical beads of diameter δ residing on the same lattice $\mathcal{L}$ as the HP1 dimers (35). The bending rigidity of the chromatin fiber was incorporated via a standard angular potential of stiffness κ,

$$\mathcal{H}_{bend} = \sum_{k=3}^{\mathcal{N}_{chr}} \kappa(1 - \cos\theta_k), \qquad (2)$$

where θ_k denotes the angle formed by the triplet of adjacent monomers $(k-2,\ k-1,\ k)$. Assuming a standard chromatin compaction value of $50\ bp/nm$, the effective chain diameter $\delta = 20\ nm$ commensurate with the typical HP1 dimer size implies that each monomer within the chain encapsulates a genomic locus of approximate length $\vartheta = 1\ kbp$. Accordingly, we set the fiber bending modulus to $\kappa = 3.217\ k_B T$, corresponding to a Kuhn length $l_K = 100\ nm$ consistent with the predictions of coarse-grained chromatin models at similar levels of spatial resolution (96, 97).

Each monomer was considered to be in one of two chromatin states, respectively depicted in red and black in Figs.2-4, in order to differentiate genomic domains bearing the H3K9me2/3 histone modifications (red) from euchromatic regions (black). The chromodomain-mediated binding affinity of HP1 for H3K9-methylated histone tails was accounted for through a short-ranged attractive potential of depth $J_{HP1-H3K9}$,

$$\mathcal{H}_{HP1-H3K9} = -J_{HP1-H3K9} \sum_{i\in\mathcal{L}} \sigma_i \sum_{j\in\mathcal{V}(i)} \pi_j^{H3K9}, \qquad (3)$$

where the occupancy number π_j^{H3K9} quantifies the number of H3K9-methylated loci present at a given lattice site j. Note that we do not account for steric hindrance between HP1 beads and chromatin monomers, and thus lattice sites may be occupied simultaneously by both types of particles. Whole chromosome simulations were performed starting from dense, random and

unknotted initial configurations, and were similarly evolved via a kinetic MC scheme, as detailed in previous work (35). In this case, each MC step consists of a number $\mathcal{N}_{chr}$ of local trial displacements involving individual monomers, including both translation and reptation moves (35). Polymer acceptance rates were computed from Eqs. (2) and (3) based on the Metropolis rule (92), and Eq. (3) was also incorporated into the Hamiltonian in Eq. (1) for the determination of HP1 acceptance probabilities in coupled chromatin-HP1 simulations. Simulation and analysis codes are available at https://github.com/physical-biology-of-chromatin/LatticePoly.

Live embryo imaging & analysis

Flies homozygous for the expression of ectopic GFP-HP1a on the second chromosome (+, GFP-HP1a/CyO; +) were allowed to lay embryos on apple juice plates supplemented with yeast paste at 25°C. Embryos were collected by hand and dechorionated in 50% bleach before being mounted for live imaging. Embryos were imaged using a Zeiss 880 Airyscan microscope with a 63x/1.4 oil immersion objective. Time-lapse image stacks were collected every 30 seconds with a Z-spacing of $0.36\ \mu m$. Imaging at least part of nuclear cycle 13 (NC 13) allowed the start of NC14 (time=0) to be clearly defined as the first time point where circular nuclei appear following mitosis. All movies were Airyscan-processed using Zen 2.3 software and the first 72 time points of NC 14 (approximately $\tau_{max} \cong 36$ minutes) were analyzed using the Arivis software. Briefly, HP1a foci were segmented from the overall nuclear signal using an intensity threshold > 75% of the fluorescence intensity and a lower size threshold of 0.03 μm^3 corresponding to approximately 10 voxels ($0.085\ \mu m \times 0.085\ \mu m \times 0.36\ \mu m$). All HP1a segments found to be percolating in 3-dimensional space were merged into a single segment, and population statistics were calculated for each time point. Imaging data will be provided upon request to the corresponding authors.

REFERENCES

1. P. Bhat, D. Honson, M. Guttman, Nuclear compartmentalization as a mechanism of quantitative control of gene expression. *Nat. Rev. Mol. Cell Biol.* **22**, 653–670 (2021).

2. M. Lisby, R. Rothstein, U. H. Mortensen, Rad52 forms DNA repair and recombination centers during S phase. *Proc. Natl. Acad. Sci. U. S. A.* **98**, 8276–8282 (2001).

3. A. Papantonis, P. R. Cook, Transcription factories: genome organization and gene regulation. *Chem. Rev.* **113**, 8683–8705 (2013).

4. B. R. Sabari, *et al.*, Coactivator condensation at super-enhancers links phase separation and gene control. *Science* **361** (2018).

5. N. Saner, *et al.*, Stochastic association of neighboring replicons creates replication factories in budding yeast. *J. Cell Biol.* **202**, 1001–1012 (2013).

6. E. R. Gibney, C. M. Nolan, Epigenetics and gene expression. *Heredity* **105**, 4–13 (2010).

7. Y. Shin, C. P. Brangwynne, Liquid phase condensation in cell physiology and disease. *Science* **357** (2017).

8. A. A. Hyman, C. A. Weber, F. Jülicher, Liquid-liquid phase separation in biology. *Annu. Rev. Cell Dev. Biol.* **30**, 39–58 (2014).

9. C. P. Brangwynne, P. Tompa, R. V. Pappu, Polymer physics of intracellular phase transitions.

Nat. Phys. **11**, 899–904 (2015).

10. D. T. McSwiggen, M. Mir, X. Darzacq, R. Tjian, Evaluating phase separation in live cells: diagnosis, caveats, and functional consequences. *Genes Dev.* **33**, 1619–1634 (2019).

11. F. Erdel, K. Rippe, Formation of Chromatin Subcompartments by Phase Separation. *Biophys. J.* **114**, 2262–2270 (2018).

12. M. L. Heltberg, J. Miné-Hattab, A. Taddei, A. M. Walczak, T. Mora, Physical observables to determine the nature of membrane-less cellular sub-compartments. *Elife* **10** (2021).

13. R. C. Allshire, H. D. Madhani, Ten principles of heterochromatin formation and function. *Nat. Rev. Mol. Cell Biol.* **19**, 229–244 (2018).

14. J. C. Eissenberg, S. C. Elgin, The HP1 protein family: getting a grip on chromatin. *Curr. Opin. Genet. Dev.* **10**, 204–210 (2000).

15. D. L. Mendez, R. E. Mandt, S. C. R. Elgin, Heterochromatin Protein 1a (HP1a) partner specificity is determined by critical amino acids in the chromo shadow domain and C-terminal extension. *J. Biol. Chem.* **288**, 22315–22323 (2013).

16. A. J. Bannister, *et al.*, Selective recognition of methylated lysine 9 on histone H3 by the HP1 chromo domain. *Nature* **410**, 120–124 (2001).

17. A. Thiru, *et al.*, Structural basis of HP1/PXVXL motif peptide interactions and HP1 localisation to heterochromatin. *EMBO J.* **23**, 489–499 (2004).

18. D. Canzio, *et al.*, Chromodomain-mediated oligomerization of HP1 suggests a nucleosome-bridging mechanism for heterochromatin assembly. *Mol. Cell* **41**, 67–81 (2011).

19. S. Machida, *et al.*, Structural Basis of Heterochromatin Formation by Human HP1. *Mol. Cell* **69**, 385–397.e8 (2018).

20. T. Cheutin, *et al.*, Maintenance of stable heterochromatin domains by dynamic HP1 binding. *Science* **299**, 721–725 (2003).

21. A. G. Larson, *et al.*, Liquid droplet formation by HP1α suggests a role for phase separation in heterochromatin. *Nature* **547**, 236–240 (2017).

22. A. R. Strom, *et al.*, Phase separation drives heterochromatin domain formation. *Nature* **547**, 241–245 (2017).

23. M. M. Keenen, *et al.*, HP1 proteins compact DNA into mechanically and positionally stable phase separated domains. *Elife* **10** (2021).

24. A. Kumar, H. Kono, Heterochromatin protein 1 (HP1): interactions with itself and chromatin components. *Biophys. Rev.* **12**, 387–400 (2020).

25. A. P. Latham, B. Zhang, Consistent Force Field Captures Homologue-Resolved HP1 Phase Separation. *J. Chem. Theory Comput.* **17**, 3134–3144 (2021).

26. D. Canzio, *et al.*, A conformational switch in HP1 releases auto-inhibition to drive heterochromatin assembly. *Nature* **496**, 377–381 (2013).

27. S. Kilic, A. L. Bachmann, L. C. Bryan, B. Fierz, Multivalency governs HP1α association dynamics with the silent chromatin state. *Nat. Commun.* **6** (2015).

28. L. Wang, *et al.*, Histone Modifications Regulate Chromatin Compartmentalization by Contributing to a Phase Separation Mechanism. *Mol. Cell* **76**, 646–659.e6 (2019).

29. M. Barbieri, *et al.*, Complexity of chromatin folding is captured by the strings and binders switch model. *Proc. Natl. Acad. Sci. U. S. A.* **109**, 16173–16178 (2012).

30. Q. MacPherson, B. Beltran, A. J. Spakowitz, Bottom–up modeling of chromatin segregation due to epigenetic modifications. *Proc. Natl. Acad. Sci. U. S. A.* **115**, 12739–12744 (2018).

31. A. Esposito, *et al.*, Polymer physics reveals a combinatorial code linking 3D chromatin architecture to 1D chromatin states. *Cell Rep.* **38**, 110601 (2022).

32. F. Erdel, *et al.*, Mouse Heterochromatin Adopts Digital Compaction States without Showing Hallmarks of HP1-Driven Liquid-Liquid Phase Separation. *Mol. Cell* **78**, 236–249.e7 (2020).

33. J. A. Riback, *et al.*, Composition-dependent thermodynamics of intracellular phase separation. *Nature* **581**, 209–214 (2020).

34. A. Zidovska, The rich inner life of the cell nucleus: dynamic organization, active flows, and emergent rheology. *Biophys. Rev.* **12**, 1093–1106 (2020).

35. S. K. Ghosh, D. Jost, How epigenome drives chromatin folding and dynamics, insights from efficient coarse-grained models of chromosomes. *PLoS Comput. Biol.* **14**, e1006159 (2018).

36. D. H. Rothman, S. Zaleski, Lattice-gas models of phase separation: interfaces, phase transitions, and multiphase flow. *Rev. Mod. Phys.* **66**, 1417–1479 (1994).

37. J. Berry, C. P. Brangwynne, M. Haataja, Physical principles of intracellular organization via active and passive phase transitions. *Rep. Prog. Phys.* **81**, 046601 (2018).

38. S. Alberti, A. Gladfelter, T. Mittag, Considerations and Challenges in Studying Liquid-Liquid Phase Separation and Biomolecular Condensates. *Cell* **176**, 419–434 (2019).

39. J.-M. Choi, A. S. Holehouse, R. V. Pappu, Physical Principles Underlying the Complex Biology of Intracellular Phase Transitions. *Annu. Rev. Biophys.* **49**, 107–133 (2020).

40. C. M. Caragine, S. C. Haley, A. Zidovska, Surface Fluctuations and Coalescence of Nucleolar Droplets in the Human Cell Nucleus. *Phys. Rev. Lett.* **121**, 148101 (2018).

41. S. F. Banani, H. O. Lee, A. A. Hyman, M. K. Rosen, Biomolecular condensates: organizers of cellular biochemistry. *Nat. Rev. Mol. Cell Biol.* **18**, 285–298 (2017).

42. D. M. Church, *et al.*, Lineage-specific biology revealed by a finished genome assembly of the mouse. *PLoS Biol.* **7**, e1000112 (2009).

43. M. Falk, *et al.*, Heterochromatin drives compartmentalization of inverted and conventional nuclei. *Nature* **570**, 395–399 (2019).

44. M. M. C. Tortora, H. Salari, D. Jost, Chromosome dynamics during interphase: a biophysical perspective. *Curr. Opin. Genet. Dev.* **61**, 37–43 (2020).

45. Y. Gao, M. Han, S. Shang, H. Wang, L. S. Qi, Interrogation of the dynamic properties of higher-order heterochromatin using CRISPR-dCas9. *Mol. Cell* **81**, 4287–4299.e5 (2021).

46. I. Solovei, K. Thanisch, Y. Feodorova, How to rule the nucleus: divide et impera. *Curr. Opin. Cell Biol.* **40**, 47–59 (2016).

47. J. H. Gibcus, J. Dekker, The Hierarchy of the 3D Genome. *Mol. Cell* **49**, 773–782 (2013).

48. D. Jost, P. Carrivain, G. Cavalli, C. Vaillant, Modeling epigenome folding: formation and dynamics of topologically associated chromatin domains. *Nucleic Acids Res.* **42**, 9553–9561 (2014).

49. D. S. W. Lee, N. S. Wingreen, C. P. Brangwynne, Chromatin mechanics dictates subdiffusion and coarsening dynamics of embedded condensates. *Nat. Phys.* **17**, 531–538 (2019).

50. Y. Shin, *et al.*, Liquid Nuclear Condensates Mechanically Sense and Restructure the Genome. *Cell* **176**, 1518 (2019).

51. Y. Qi, B. Zhang, Chromatin network retards nucleoli coalescence. *Nat. Commun.* **12**, 6824 (2021).

52. , A. J. Webster, M. E. Cates, Stabilization of Emulsions by Trapped Species. *Langmuir* **14**, 2068 (1998).

53. W. Xu, Z. Lan, B. Peng, R. Wen, X. Ma, Evolution of transient cluster/droplet size distribution in a heterogeneous nucleation process. *RSC Adv.* **4**, 31692–31699 (2014).

54. K. H.-C. Wei, C. Chan, D. Bachtrog, Establishment of H3K9me3-dependent heterochromatin during embryogenesis in Drosophila miranda. *eLife* **10** (2021).

55. C. D. Smith, S. Shu, C. J. Mungall, G. H. Karpen, The Release 5.1 annotation of Drosophila melanogaster heterochromatin. *Science* **316**, 1586–1591 (2007).

56. J. Bonnet, *et al.*, Quantification of Proteins and Histone Marks in Drosophila Embryos Reveals Stoichiometric Relationships Impacting Chromatin Regulation. *Dev. Cell* **51**, 632–644.e6 (2019).

57. K. Yuan, P. H. O'Farrell, TALE-light imaging reveals maternally guided, H3K9me2/3-independent emergence of functional heterochromatin in Drosophila embryos. *Genes Dev.* **30**, 579–593 (2016).

58. C. A. Seller, C.-Y. Cho, P. H. O'Farrell, Rapid embryonic cell cycles defer the establishment of heterochromatin by Eggless/SetDB1 in Drosophila. *Genes Dev.* **33**, 403–417 (2019).

59. D. Bracha, M. T. Walls, C. P. Brangwynne, Probing and engineering liquid-phase organelles. *Nat. Biotechnol.* **37**, 1435–1445 (2019).

60. J.-U. Sommer, H. Merlitz, H. Schiessel, Polymer-assisted condensation: A mechanism for hetero-chromatin formation and epigenetic memory. *Macromolecules* **55**, 4841–4851 (2022).

61. A. Pancholi, *et al.*, RNA polymerase II clusters form in line with surface condensation on regulatory chromatin. *Mol. Syst. Biol.* **17**, e10272 (2021).

62. J. A. Morin, *et al.*, Surface condensation of a pioneer transcription factor on DNA. https:/doi.org/10.1101/2020.09.24.311712.

63. I. Malhotra, B. Oyarzún, B. M. Mognetti, Unfolding of the chromatin fiber driven by overexpression of noninteracting bridging factors. *Biophys. J.* **120**, 1247–1256 (2021).

64. J.-M. Choi, F. Dar, R. V. Pappu, LASSI: A lattice model for simulating phase transitions of multivalent proteins. *PLoS Comput. Biol.* **15**, e1007028 (2019).

65. Y. Zhang, D. S. W. Lee, Y. Meir, C. P. Brangwynne, N. S. Wingreen, Mechanical Frustration of Phase Separation in the Cell Nucleus by Chromatin. *Phys. Rev. Lett.* **126**, 258102 (2021).

66. S. Sati, *et al.*, 4D Genome Rewiring during Oncogene-Induced and Replicative Senescence. *Mol. Cell* **78**, 522–538.e9 (2020).

67. I. Eshghi, J. A. Eaton, A. Zidovska, Interphase Chromatin Undergoes a Local Sol-Gel Transition upon Cell Differentiation. *Phys. Rev. Lett.* **126**, 228101 (2021).

68. G. LeRoy, *et al.*, Heterochromatin protein 1 is extensively decorated with histone code-like post-translational modifications. *Mol. Cell. Proteomics* **8**, 2432–2442 (2009).

69. M. Jagannathan, R. Cummings, Y. M. Yamashita, The modular mechanism of chromocenter formation in Drosophila. *eLife* **8**, e43938 (2019).

70. G. Gerlitz, The Emerging Roles of Heterochromatin in Cell Migration. *Front Cell Dev Biol* **8**, 394 (2020).

71. Y. Feodorova, M. Falk, L. A. Mirny, I. Solovei, Viewing Nuclear Architecture through the Eyes of Nocturnal Mammals. *Trends Cell Biol.* **30**, 276–289 (2020).

72. P. Cruz-Tapias, P. Robin, J. Pontis, L. D. Maestro, S. Ait-Si-Ali, The H3K9 Methylation Writer SETDB1 and its Reader MPP8 Cooperate to Silence Satellite DNA Repeats in Mouse Embryonic Stem Cells. *Genes* **10** (2019).

73. A. R. Cutter DiPiazza, *et al.*, Spreading and epigenetic inheritance of heterochromatin require a critical density of histone H3 lysine 9 tri-methylation. *Proc. Natl. Acad. Sci. U. S. A.* **118** (2021).

74. M. J. Obersriebnig, E. M. H. Pallesen, K. Sneppen, A. Trusina, G. Thon, Nucleation and spreading of a heterochromatic domain in fission yeast. *Nat. Commun.* **7**, 11518 (2016).

75. D. Jost, C. Vaillant, P. Meister, Coupling 1D modifications and 3D nuclear organization: data, models and function. *Curr. Opin. Cell Biol.* **44**, 20–27 (2017).

76. D. Jost, C. Vaillant, Epigenomics in 3D: importance of long-range spreading and specific interactions in epigenomic maintenance. *Nucleic Acids Res.* **46**, 2252–2264 (2018).

77. D. Michieletto, E. Orlandini, D. Marenduzzo, Polymer model with epigenetic recoloring reveals a pathway for the de novo establishment and 3D organization of chromatin domains. *Phys. Rev. X* **6**, 041047 (2016).

78. S. H. Sandholtz, Q. MacPherson, A. J. Spakowitz, Physical modeling of the heritability and maintenance of epigenetic modifications. *Proc. Natl. Acad. Sci. U. S. A.* **117**, 20423–20429 (2020).

79. A. Rosa, R. Everaers, Structure and dynamics of interphase chromosomes. *PLoS Comput. Biol.* **4**, e1000153 (2008).

80. W. F. Marshall, A. F. Dernburg, B. Harmon, D. A. Agard, J. W. Sedat, Specific interactions of chromatin with the nuclear envelope: positional determination within the nucleus in Drosophila melanogaster. *Mol. Biol. Cell* **7**, 825–842 (1996).

81. G. Nishibuchi, J.-I. Nakayama, Biochemical and structural properties of heterochromatin protein 1: understanding its role in chromatin assembly. *J. Biochem.* **156**, 11–20 (2014).

82. D. Canzio, A. Larson, G. J. Narlikar, Mechanisms of functional promiscuity by HP1 proteins. *Trends Cell Biol.* **24**, 377–386 (2014).

83. S. Guha, M. K. Mitra, Multivalent binding proteins can drive collapse and reswelling of chromatin in confinement. https:/doi.org/10.1101/2022.01.21.477199.

84. S. Maharana, *et al.*, RNA buffers the phase separation behavior of prion-like RNA binding proteins. *Science* **360**, 918–921 (2018).

85. E. M. Langdon, *et al.*, mRNA structure determines specificity of a polyQ-driven phase separation. *Science* **360**, 922–927 (2018).

86. A. Janssen, *et al.*, A single double-strand break system reveals repair dynamics and mechanisms in heterochromatin and euchromatin. *Genes Dev.* **30**, 1645–1657 (2016).

87. F. Zenk, *et al.*, HP1 drives de novo 3D genome reorganization in early Drosophila embryos. *Nature* **593**, 289–293 (2021).

88. Y. C. G. Lee, *et al.*, Pericentromeric heterochromatin is hierarchically organized and spatially contacts H3K9me2 islands in euchromatin. *PLoS Genet.* **16**, e1008673 (2020).

89. B. Schuettengruber, H.-M. Bourbon, L. Di Croce, G. Cavalli, Genome Regulation by Polycomb and Trithorax: 70 Years and Counting. *Cell* **171**, 34–57 (2017).

90. A. J. Plys, *et al.*, Phase separation of Polycomb-repressive complex 1 is governed by a charged disordered region of CBX2. *Genes Dev.* **33**, 799–813 (2019).

91. E. Seif, *et al.*, Phase separation by the polyhomeotic sterile alpha motif compartmentalizes Polycomb Group proteins and enhances their activity. *Nat. Commun.* **11**, 5609 (2020).

92. K. Binder, *Monte Carlo Methods in Statistical Physics* (Springer Science & Business Media, 2012).

93. M. A. Katsoulakis, D. G. Vlachos, Coarse-grained stochastic processes and kinetic Monte Carlo simulators for the diffusion of interacting particles. *J. Chem. Phys.* **119**, 9412–9427 (2003).

94. H. Hajjoul, *et al.*, High-throughput chromatin motion tracking in living yeast reveals the flexibility of the fiber throughout the genome. *Genome Res.* **23**, 1829–1838 (2013).

95. A. G. Kikhney, D. I. Svergun, A practical guide to small angle X-ray scattering (SAXS) of flexible and intrinsically disordered proteins. *FEBS Lett.* **589**, 2570–2577 (2015).

96. J.-M. Arbona, S. Herbert, E. Fabre, C. Zimmer, Inferring the physical properties of yeast chromatin through Bayesian analysis of whole nucleus simulations. *Genome Biol.* **18**, 81 (2017).

97. M. Socol, *et al.*, Rouse model with transient intramolecular contacts on a timescale of seconds recapitulates folding and fluctuation of yeast chromosomes. *Nucleic Acids Res.* **47**, 6195–6207 (2019).